Cancer Nanotechnology

REVIEW Open Access

Development of a novel nanoformulation based on aloe vera-derived carbon quantum dot and chromium-doped alumina nanoparticle (Al_2O_3:Cr@Cdot NPs): evaluating the anticancer and antimicrobial activities of nanoparticles in photodynamic therapy

Merat Karimi[1], Mina Homayoonfal[2], Mostafa Zahedifar[1,3], Amirreza Ostadian[4], Reyhaneh Adibi[3], Bahareh Mohammadzadeh[1], Arash Raisi[5], Fatemeh Ravaei[5], Somaye Rashki[6], Mahsa Khakbraghi[7], Michael Hamblin[8], Zahra Kheirkhah[1], Ehsan Sadeghi[1,3*], Majid Nejati[9*] and Hamed Mirzaei[2*]

*Correspondence:
sdgh@kashanu.ac.ir;
mnejatimt@gmail.com;
mirzaei-h@kaums.ac.ir;
h.mirzaei2002@gmail.com

[2] Research Center for Biochemistry and Nutrition in Metabolic Diseases, Institute for Basic Sciences, Kashan University of Medical Sciences, Kashan, Iran
[3] Department of Physics, University of Kashan, Kashan, Isfahan, Iran
[9] Anatomical Sciences Research Center, Institute for Basic Sciences, Kashan University of Medical Sciences, Kashan, Iran
Full list of author information is available at the end of the article

Abstract

The objective of this study was to synthesize a novel antibacterial and anticancer nanoformulation using aloe vera-derived carbon quantum dots (Cdot) and chromium-doped alumina nanoparticles (Al_2O_3:Cr/Cdot NPs) via a sol–gel method. X-ray diffraction (XRD) analysis confirmed crystalline NPs with a size range of 10–12 nm, while energy-dispersive X-ray spectroscopy (EDS) revealed their elemental composition without impurities. Fourier-transform infrared spectroscopy (FT-IR) indicated strong interactions between Cdot and Al_2O_3:Cr NPs, forming a robust heterostructure. Scanning electron microscopy (SEM) and transmission electron microscopy (TEM) images provided visual confirmation of monodisperse, spherical NPs, ensuring uniformity for further applications. Evaluation of reactive oxygen species (ROS) demonstrated superior generation of singlet oxygen and hydroxyl radicals by Al_2O_3:Cr/Cdot NPs, essential for photodynamic therapy. Minimum inhibitory concentration (MIC) tests revealed potent antibacterial activity against drug-resistant bacteria, inhibiting biofilm formation by 89% and 95% for MRSA and *P. aeruginosa* PAO1, respectively. Furthermore, the anticancer activity of Al_2O_3:Cr/Cdot NPs was assessed using C26 cells, demonstrating enhanced cytotoxicity upon UVA exposure. The NPs exhibited an inhibitory concentration (IC50) of 20 µg/mL without UVA exposure, decreasing to 10 µg/mL with UVA exposure, highlighting the synergistic effect of UVA light in enhancing cytotoxicity. Overall, these findings underscore the significant potential of Al_2O_3:Cr/Cdot NPs as multifunctional agents for addressing drug-resistant bacteria and advancing cancer therapy, offering promising avenues for nanomedicine research and development.

Keywords: Chromium-doped Al_2O_3 nanoparticles, Carbon quantum dot, Photodynamic therapy, Singlet oxygen, Hydroxyl radical, Antibacterial activity, Cancer therapy

Introduction

In recent years, addressing infectious diseases has become increasingly challenging for public health due to the emergence of bacterial resistance to antibiotics, leading to extended hospital stays, increased healthcare expenses, and elevated mortality rates (Chinemerem Nwobodo et al. 2022). Among the mechanisms contributing to bacterial resistance, biofilm formation stands out as a primary factor exacerbating drug resistance, posing significant challenges in treating biofilm-related infections. Biofilms, composed of bacteria encased in a matrix, present in various medical conditions such as chronic wounds, chronic obstructive pulmonary disease (COPD), urinary tract infections (UTIs), and cystic fibrosis, significantly augmenting antibiotic resistance compared to their planktonic form (Dutt et al. 2022; Wu et al. 2021). Therefore, discovering and characterizing innovative methods as novel antibiofilm agents is imperative for preventing and treating bacterial biofilms (Vuotto and Donelli 2019). In this context, nanomaterials have garnered considerable attention for their potential in combating bacterial proliferation. Metal oxide nanoparticles (NPs), including zinc oxide, iron oxide, titanium dioxide, silver oxide, and copper oxide, have shown promise in inhibiting bacterial growth (Ramasamy and Lee 2016; Khan et al. 2014, 2016; Umar et al. 2022). Aluminum oxide (Al_2Ox) NPs have emerged as potent agents against drug-resistant bacteria and cancer, with even low concentrations exhibiting strong antibacterial effects (Gudkov et al. 2022). The release of Al^{3+} ions from Al_2O_3 NPs triggers the generation of reactive oxygen species (ROS), which in turn damages cellular components such as nucleic acids, proteins, and lipids (Jwad et al. 2019). Similarly, Chromium oxide NPs (Cr_2O_3 NPs) have demonstrated significant biomedical applications due to their unique physicochemical properties, including potent antioxidant, antibacterial, anticancer, antiviral, and antidiabetic properties (Ahmed Mohamed et al. 2020; Ramesh et al. 2012).

Carbon quantum dots (Cdot) have also attracted attention for their potential in combating bacteria, owing to their compatibility with living organisms, facile manufacturing process, tunability, and diverse functional properties (Hao et al. 2021). It is hypothesized that positively charged Cdot interacts with bacterial cell membranes, disrupting membrane permeability and ultimately causing cell death. Additionally, Cdot induces oxidative stress in the bacterial cell wall, leading to damage to membrane proteins and DNA, ultimately resulting in cell death (Anand et al. 2019). Cdot has recently garnered significant interest in cancer treatment due to its exceptional attributes, such as biocompatibility, minimal cytotoxicity, water solubility, and distinct photoluminescence (Prasad et al. 2016). Cdot and their composites have demonstrated potential for cancer therapy through phototherapy and radiotherapy. For example, in photodynamic therapy, Cdot suppressed the growth of human breast cancer cells MCF-7 and MDA-MB-231 by inducing the generation of singlet oxygen species (Hsu et al. 2013).

Common cancer treatment methods, including chemotherapy, radiotherapy, immunotherapy, and surgery, have drawbacks like toxicity, lack of specificity, and incomplete tumor removal. Photodynamic therapy (PDT) is suggested as an alternative, generating

reactive oxygen species (ROS) to damage cells and tissues using photosensitizer drugs and light irradiation (Dolmans et al. 2003; Hong et al. 2016). However, the effectiveness of PDT is primarily limited to treating superficial cancerous tissues. In recent years, nanotechnology has provided groundbreaking solutions in materials science, electronics, and medicine by exploiting unique NPs properties (Tavakkoli et al. 2018). Nanotechnology enhances PDT research by optimizing photosensitizers and providing selective tumor targeting through the enhanced permeability and retention effect. Cdot emerges as a promising candidate for PDT advancement (Karagianni et al. 2023). This study aimed to synthesize a novel nanocomposite consisting of Aloe vera-derived Cdot and Cr-doped aluminum oxide nanoparticles (Al_2O_3:Cr NPs), designated as Al_2O_3:Cr/Cdot NPs, via a sol–gel approach, and assess their suitability for PDT. The characteristics of the prepared NPs were investigated using X-ray diffraction (XRD), energy-dispersive X-ray spectroscopy (EDS), Fourier-transform infrared spectroscopy (FTIR), transmission electron microscopy (TEM), and scanning electron microscopy (SEM). Additionally, the Al_2O_3:Cr/Cdot NPs were evaluated for their antibacterial and antibiofilm potential, in combination with PDT, against both Gram-positive (methicillin-resistant *Staphylococcus aureus*) and Gram-negative (*Pseudomonas aeruginosa PAO1*) bacteria. Finally, the fabricated NPs were assessed in C26 colon cancer cell lines, along with their potential for PDT effects. By exploring the synergistic effects of Aloe vera-derived Cdot and Cr-doped aluminum oxide NPs, this study aims to contribute to the development of innovative strategies for combating antibiotic resistance and advancing cancer therapy.

Materials and methods

Materials

In this study, analytical grade aluminum nitrate [Al $(NO_3)_3 \cdot 9H_2O$], oleic acid ($C_{18}H_{34}O_2$), chromium nitrate [Cr $(NO_3)_3$], anthracene ($C_{14}H_{10}$), crystal violet, methylene blue ($C_{16}H_{18}ClN_3S$) ethanol, methanol, and glacial acetic acid were purchased from Merck and utilized without additional purification. Moreover, the required Mueller Hinton broth, Mueller Hinton Agar, and Tryptic Soy Broth were obtained from Merck.

Synthesis of Cr-doped Al_2O_3 NPs

To prepare Cr-doped Al_2O_3 NPs, a sol–gel method was employed. Initially, 3.750 g of aluminum nitrate and two mole% of chromium nitrate were mixed with 10 mL of deionized water and stirred on a magnetic stirrer for 60 min at room temperature (25 °C) to form a homogenized sol. During this stage, the aluminum and chromium ions dissolved in the aqueous solution undergo hydrolysis, leading to the formation of aluminum hydroxide and chromium hydroxide precursors. Subsequently, oleic acid was added at a volume ratio of 2:1 to the solution. Oleic acid serves as a surfactant and stabilizer, facilitating the uniform dispersion of the metal ions in the solution. The mixture was then stirred at 3000 rpm for 4 h at 25 °C to ensure thorough mixing and interaction between the precursors. The excess liquid was evaporated by heating the solution at 250 °C for 6 h, resulting in the formation of a black gel. This gel consists of the aggregated metal hydroxide particles. Finally, the black gel was calcined at 800 °C to induce a series of chemical reactions, including dehydration, dehydroxylation, and crystallization. These reactions transform the amorphous gel into crystalline Cr-doped Al_2O_3 NPs, with

chromium ions incorporated into the aluminum oxide lattice structure (Karimi et al. 2021).

Preparation of carbon quantum dot nanoparticles

A Cdot nanostructure was synthesized using Aloe vera and the hydrothermal technique. Initially, 5 g of the plant material were mixed with 30 mL of deionized water and stirred continuously for 60 min until fully dissolved. Subsequently, the resulting solution was transferred to an autoclave and heated in an oven set to 180 °C for 12 h. During this hydrothermal reaction, the organic compounds present in the Aloe vera extract underwent decomposition and carbonization, leading to the formation of small carbon nanoparticles or quantum dots. After completion of the chemical reaction, the mixture was filtered through filter paper to remove any remaining particles, and the resulting solution was then refrigerated at 4 °C to stabilize the synthesized Cdot and prevent further aggregation or degradation (Raikwar 2022).

Synthesis of Cr-doped Al_2O_3-carbon quantum dot nanoparticles (Al_2O_3:Cr/Cdot NPs)

The synthesis of Al_2O_3:Cr/Cdot NPs involved a reflux reaction process. Initially, a flask containing 150 mg of Cdot) and 100 mg of Al_2O_3:Cr NPs in 5 mL of water was prepared. This mixture was then placed in an oil bath and heated to 45 °C using a stirrer heater to maintain a constant temperature. During reflux, the reaction proceeded as follows: at the interface between the Cdot and Al_2O_3:Cr NPs, surface interactions occurred, facilitating the exchange of ions and functional groups. This interaction initiated chemical bonding reactions, including covalent bonding, electrostatic interactions, and coordination bonds, between the carbon atoms of the Cdot and the metal atoms of the Al_2O_3:Cr NPs. As the reaction progresses, chromium ions (Cr^{3+}) from Al_2O_3:Cr NPs were incorporated into Cdot, resulting in the formation of Al_2O_3:Cr/Cdot. This doping process introduced specific electronic properties and functionalities to the Cdot. The reflux conditions ensured thorough mixing and uniform distribution of the NPs in the reaction mixture, promoting the growth of Al_2O_3:Cr/Cdot through the deposition of additional atoms and molecules onto their surface. This growth process may also involve the aggregation of individual nanoparticles to form larger clusters. Finally, the resulting mixture was dried in an oven at 80 °C for 12 h to remove excess solvent and promote the formation of solid Al_2O_3:Cr/Cdot NPs. This drying process helped consolidate the NPs and enhanced their stability for subsequent characterization and applications.

Characteristics of NPs

In the present study, the investigation aimed to comprehensively characterize the structural and chemical properties of the synthesized NPs using various analytical techniques. X-ray diffraction (XRD) measurements were conducted to determine the crystalline nature of the NPs. XRD analysis is essential for identifying the crystal structure and phase composition of nanomaterials. The XRD analysis was performed using a Philips X'pert Pro MPP model instrument equipped with Cu Kα radiation and a Ni filter, with a wavelength of 0.1540 nm. Fourier-transform infrared (FT-IR) spectroscopy was employed to elucidate the existence of specific functional groups within the NPs. This technique provides valuable information about the chemical bonding and functional

groups present in nanomaterials. The FT-IR analysis was carried out using a Nicolet Magna–IR550 spectrometer with KBr pellets. Scanning electron microscopy (SEM) coupled with energy-dispersive X-ray spectroscopy (EDX) was utilized to analyze particle morphology, size engineering, and elemental composition. SEM imaging provides high-resolution images of the NPs surface, while EDX enables elemental analysis of the NPs. Additionally, transmission electron microscopy (TEM) imaging, performed using a Zeiss EM900 model TEM, which provided further insights into the morphology and size distribution of the NPs at the nanoscale level. Dynamic light scattering (DLS) analysis, conducted using equipment from Vasco, Cordouan Technologies, France, was employed to measure the size of the NPs and obtain information about their particle distribution. DLS is a crucial technique for determining the hydrodynamic diameter and size distribution of NPs in solution. UV–Vis spectroscopy was employed to evaluate the optical properties of the synthesized NPs. This technique provides information about the absorption and optical characteristics of nanomaterials, aiding in their characterization. The analysis was performed using a PHYSTEC/Iran UVS-2500 spectrometer, covering a wavelength range from 200 to 800 nm, in a temperature-stable environment. These analytical methods, including XRD, FT-IR, SEM–EDX, TEM, DLS, and UV–Vis spectroscopy, collectively provided comprehensive insights into the structural and chemical characteristics of the synthesized NPs. Understanding these properties is essential for assessing their suitability and potential applications in various fields, including antibacterial and anticancer therapies.

Measurement of reactive oxygen species (ROS)

In PDT, tumor destruction is achieved by generating reactive singlet oxygen or radical compounds. Despite the abundance of free radicals in the environment, only a few, such as hydroxyl and superoxide, are produced in the body, making their detection challenging due to their short lifespan. Fluorescence-based methods with suitable probes offer a precise means of detecting ROS due to their high sensitivity and simplicity, ensuring the acquisition of reliable data. In this study, two detectors, anthracene and methylene blue, were utilized to identify ROS.

In this study, anthracene, a commonly used fluorescent agent for tracking singlet oxygen molecules, served as the detector for singlet oxygen. Upon oxidation by singlet oxygen, anthracene transforms into non-fluorescent anthraquinone. To prepare the solution, 1 mg of anthracene was dissolved in ethanol. Subsequently, 0.03 mL of the anthracene solution was added to the NP solution in the absence of light. The absorbance spectrum of anthracene was then analyzed using an ultraviolet–visible spectrophotometer. Then, the mixture was exposed to UVA light (320–400 nm) for one hour to induce the cyclo-addition of anthracene. The absorbance spectrum was reassessed, and the amount of singlet oxygen molecules formed was determined by measuring the decrease in absorbance intensity.

To detect the presence of free radicals, methylene blue (MB) was employed as a detector. Initially, 1 mg of MB was mixed with 50 mL of pure water. Subsequently, 1.5 mL of this solution was added to the NP samples at a neutral pH. The absorbance spectrum of MB was recorded using a UV–vis spectrophotometer. Then, the samples were exposed to UVC light (200–290 nm) for 40 min, after which their absorbance spectrum was

observed again. The number of hydroxyl radicals produced was determined by measuring the decrease in absorbance density.

Evaluation of the antibacterial activity of NPs

The antibacterial activity of the synthesized NPs (Al_2O_3:Cr, Cdot, and Al_2O_3:Cr/Cdot) was evaluated through various assays, including minimum inhibitory concentration (MIC) tests, minimum bactericidal concentration (MBC) tests and assessment of anti-biofilm activity against methicillin-resistant *Staphylococcus aureus ATCC43300* (MRSA) and *Pseudomonas aeruginosa PAO1*.

Determining the minimum inhibitory concentration (MIC)

The MIC was determined following the protocols established by the Clinical and Laboratory Standards Institute (CLSI), utilizing the broth microdilution technique. Initially, 100 µL of sterile Mueller Hinton broth (MHB) was dispensed into each well of a sterile 96-well plate, followed by the addition of a dilution series of the NPs to the wells. Subsequently, 10 µL of the bacterial solution containing approximately 5×10^5 colony-forming units (CFU) was inoculated into the wells. The plate was then incubated at 37 °C for 18–20 h. The lowest concentration of NPs that prevented bacterial growth was recorded as the MIC (Safardoust-Hojaghan et al. 2021).

Determining the minimum bactericidal concentration (MBC)

The minimum bactericidal concentration (MBC) was determined using the broth microdilution method. Briefly, 10 µL aliquots from wells where bacterial growth was not observed were transferred to Mueller Hinton Agar (MHA) plates and incubated at 37 °C for 24 h. Subsequently, the number of CFUs was enumerated, with the MBC defined as the lowest concentration of NPs capable of reducing the bacterial population by 99.9% (Babaei et al. 2022).

Anti-biofilm activity assessment of Al_2O_3:Cr/Cdot NPs against MRSA and P. aeruginosa PAO1

To evaluate the anti-biofilm activity of Al_2O_3:Cr/Cdot NPs against MRSA and *P. aeruginosa PAO1*, bacterial cultures were incubated in Tryptic Soy Broth (TSB) containing 1% glucose for 24 h at 37 °C in the presence and absence of various concentrations of Al_2O_3:Cr/Cdot NPs (1/8 MIC, 1/4 MIC, 1/2 MIC, and MIC). After incubation, the culture medium was removed, and the wells containing biofilms were washed twice with normal saline. Subsequently, the biofilms were fixed with 150 µL of 99% methanol and air-dried at room temperature. The fixed biofilms were stained with 0.1% crystal violet for 15 min, followed by two washing cycle with distilled water. The plates were allowed to dry, and then 200 µL of 33% glacial acetic acid was added to dissolve the bound dye. The absorbance was measured at 570 nm using a microplate reader (Karami et al. 2021). Three independent experiments were conducted for each sample and the absorbance values (OD) were reported as average ± standard deviation (SD).

$$\text{Percentage of biofilm inhibition} = \frac{\text{Control OD} - \text{Test OD}}{\text{Control OD}} \times 100.$$

MTT assay

The MTT assay relies on the reduction of MTT (3-(4,5-dimethylthiazol-2-yl)-2,5-diphenyltetrazolium bromide) by viable cells to form formazan crystals, a reaction catalyzed by mitochondrial enzymes. These formazan crystals are insoluble and have a purple color. After the incubation period, the formazan crystals were solubilized using an appropriate solvent, and the absorbance of the resulting solution was measured spectrophotometrically at 570 nm. The amount of formazan produced is directly proportional to the number of viable cells in the sample, allowing for the assessment of cell viability and cytotoxicity in response to the nanoparticles.

The MTT assay was utilized to evaluate the anticancer properties and determine the IC50 of Al_2O_3:Cr/Cdot nanoparticles, as well as to assess the PDT effect. Initially, cells were exposed to varying durations of UVA light (5, 10, 20, and 30 min) to optimize the UVA exposure length for measuring the photodynamic effect, with 10 min being identified as the optimal duration. Subsequently, the C26 cell line was cultured in a 96-well plate and diluted to six concentrations of nanoparticles (10, 20, 40, 80, 160, and 320 µM). Following cell seeding, the plate was washed and then incubated at 37 °C in DMEM for 48 h to allow for NPs-cell interactions. After the incubation period, 20 µL of MTT solution was added to each well, and the plate was further incubated at the same temperature for 4 h. Subsequently, the MTT medium was substituted with 100 µL of dimethyl sulfoxide (DMSO). After a 30-min interval, the absorbance of the blue formazan at 570 nm was assessed to determine the IC_{50} value, representing the extent of cytotoxicity.

Result and discussion

Characterization of nanoparticles

XRD

Figure 1 illustrates the XRD pattern of Cdot, indicating the presence of a minute carbogenic core, as evidenced by the prominent (002) peak observed at 19° (2θ). This observation suggests a crystalline structure within the Cdot. Upon calcination of the

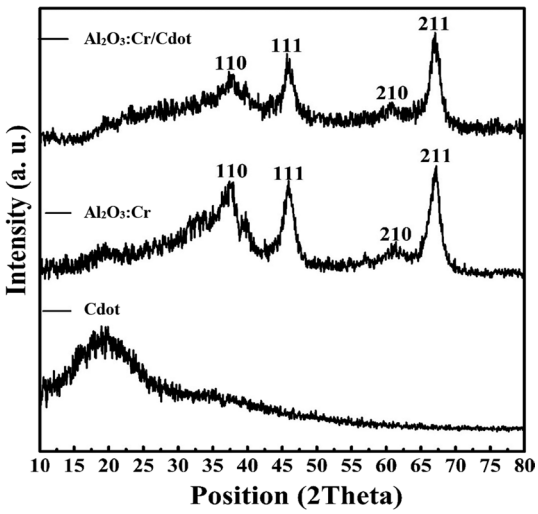

Fig. 1 XRD pattern of fabricated Cdot, Al_2O_3:Cr and Al_2O_3:Cr/Cdot nanoparticles

Al_2O_3:Cr NPs at 800 °C, distinct peaks were observed in the XRD pattern at 2θ values of 36.2°, 41.4°, 62.3°, and 67.8°, corresponding to the Al_2O_3 (110), Al_2O_3 (111), Al_2O_3 (210), and Al_2O_3 (211) planes, according to JCPDS card number 00-001-1303. It suggests the successful formation of crystalline Al_2O_3:Cr NPs. Furthermore, the XRD pattern of the Al_2O_3:Cr/Cdot nanocomposite exhibited prominent peaks at 2θ values of 36.4°, 41.6°, 62.5°, and 68°. These peaks corresponded to the Al_2O_3 (110), Al_2O_3 (111), Al_2O_3 (210), and Al_2O_3 (211) planes (JCPDS card no. 00-001-1303), respectively, suggesting their presence on the surface of the Cdot. Both the XRD patterns of Al_2O_3:Cr/Cdot NPs and the application of the Scherer formula suggest a crystallite size of approximately 10–12 nm without the presence of other phases. The Scherer formula estimated the crystallite size of the Cdot to be 5 nm, while the lattice parameter of the (211) plane was determined to be $a = 2.89$ Å, providing an average calculated crystallite size of 10 nm. These findings indicate a uniform crystalline structure within the synthesized material.

EDS

Additionally, energy-dispersive X-ray spectroscopy (EDS) was employed to analyze the elemental composition of the NPs. The EDS spectrum of the Cdot (Fig. 2a) revealed a composition of 66.2% oxygen and 33.98% carbon atoms, confirming the carbogenic nature of the Cdot. In contrast, the EDS spectrum of the Al_2O_3:Cr NPs (Fig. 2b) exhibited a composition comprising 64.66% aluminum, 34.87% oxygen, and 0.47% chromium atoms, indicative of the presence of aluminum oxide and chromium species. Finally, the EDS spectrum of the Al_2O_3:Cr/Cdot NPs (Fig. 2c) displayed peaks corresponding to aluminum, oxygen, chromium, and carbon atoms, with no other impurities detected, affirming the successful synthesis of the desired nanocomposite material.

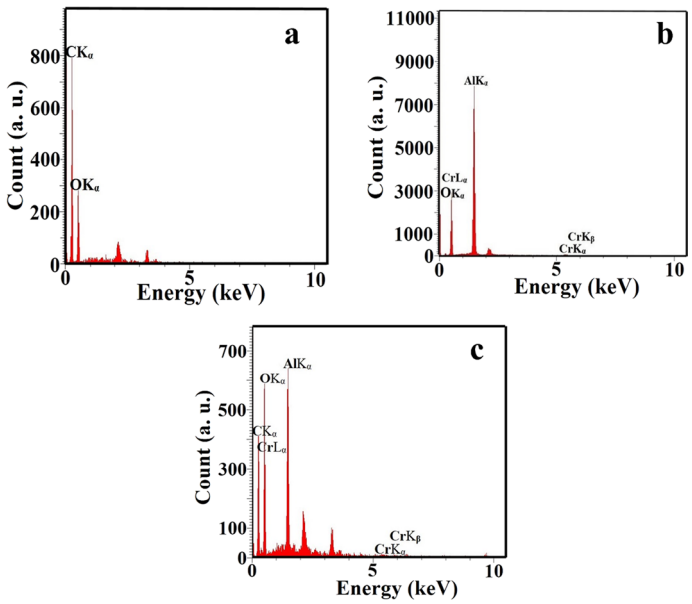

Fig. 2 EDS analysis of fabricated **a** Cdot, **b** Al_2O_3:Cr and **c** Al_2O_3:Cr/Cdot nanoparticles

FTIR

FT-IR spectroscopy serves as a valuable method for analyzing the interactions between materials and infrared light. This technique involves directing infrared waves at the NP samples, inducing changes in bond vibrations and resulting in the absorption of specific wavenumbers corresponding to chemical bonds. For this study, the absorption bands within the wavenumber range of 4000 to 500 cm^{-1} were examined.

The FT-IR spectra of Cdot, Al_2O_3:Cr NPs, and Al_2O_3:Cr nanoparticles combined with Cdot are depicted in Fig. 3. The FT-IR spectrum of Cdot (Fig. 3a) reveals the presence of several distinct types of functional groups on the surface. Broad peaks observed at 3439 and 2985 cm−^{1} can be attributed to O–H and C–H (methyl or methylene) functional groups present in aliphatic hydrocarbons, while a peak at 1733 cm^{-1} corresponds to the C=O groups on the surfaces of Cdot. Additionally, a band at 1380 cm^{-1} is associated with C–H bending bonds (Prathumsuwan et al. 2018; Sarkar et al. 2017). The wavenumber range of 400 to 1500 cm^{-1}, known as the fingerprint region, exhibits specific molecular vibrations characteristic of the materials under study. The IR signal detected at 1206 cm^{-1} is attributed to C–O stretching. Wavenumbers below 900 cm^{-1} present challenges in interpretation due to their highly complex structural signatures (Algarra et al. 2018). Furthermore, the band observed at 803 cm^{-1} represents stretching of the C-H bonds, while the band at 597 cm^{-1} is associated with lateral bending of the C–H bonds. In the FTIR spectrum of Al_2O_3:Cr NPs (Fig. 3b), the broad transmittance bands observed at 3459 cm^{-1} are attributed to OH stretching vibration groups, while the bands at 1644 and 567 cm^{-1} are assigned to H_2O bending and Al-O, respectively (Adamczyk and Długoń 2012). In the FTIR spectrum of Al_2O_3:Cr/Cdot NPs (Fig. 3c), the absence of wide absorption bands, typically corresponding to methyl or methylene groups and C=O bonds, suggests successful bonding between the Cdot and the Al_2O_3:Cr NPs. Moreover, noticeable shifts in the positions of C=O, O–H, C–H, and C–O bonds in Al_2O_3:Cr/Cdot NPs compared to Cdot and Al_2O_3:Cr indicate specific interactions between them. The emergence of two new peaks in Al_2O_3:Cr/Cdot NPs at 1074 cm^{-1} and 663 cm^{-1}, associated with C–O stretching and C=C bending bonds, respectively, illustrates the incorporation of Cdot within the Al_2O_3:Cr NPs. Hence, the shifts and alterations in the intensity

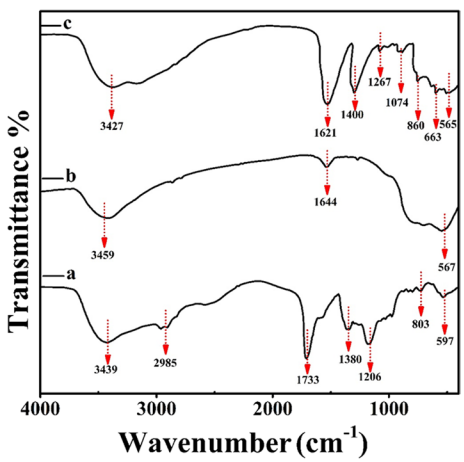

Fig. 3 FT-IR analysis of fabricated **a** Cdot, **b** Al_2O_3:Cr and **c** Al_2O_3:Cr/Cdot nanoparticles

of IR bands can be ascribed to the formation of intermolecular interactions between the components.

Morphology and particle size

The structural and morphological characteristics of the NPs were investigated using various analytical techniques. SEM analysis provided insights into the dimensions, morphology, and structure of the NPs. The SEM images for both Cdot (Fig. 4a) and Al_2O_3:Cr NPs (Fig. 4b) depict diverse shapes, including conical, spherical, and floral designs. Notably, the presence of oleic acid appeared to act as a surfactant, contributing to the formation of a uniform and thin NPs film on the sample surface. The SEM image of Al_2O_3:Cr/Cdot NPs (Fig. 4c) exhibited well-defined spherical NPs with minimal agglomeration, indicating the successful synthesis of the composite material. TEM imaging was employed to assess the size distribution of the synthesized NPs. The TEM image (Fig. 5) further confirmed the spherical shape and monodisperse nature of the NPs, with no significant aggregation observed. Particle size distribution data (Fig. 6) revealed that all NPs displayed monodispersity, characterized by a narrow size distribution without noticeable agglomeration. The average particle diameter for Cdot, Al_2O_3:Cr, and Al_2O_3:Cr/Cdot was approximately 4 nm, 6 nm, and 15 nm, respectively. These findings align with

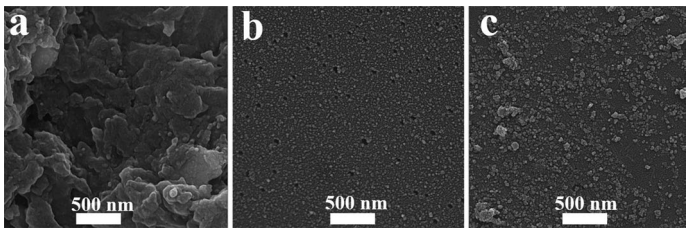

Fig. 4 SEM images of fabricated **a** Cdot, **b** Al_2O_3:Cr and **c** Al_2O_3:Cr/Cdot nanoparticles

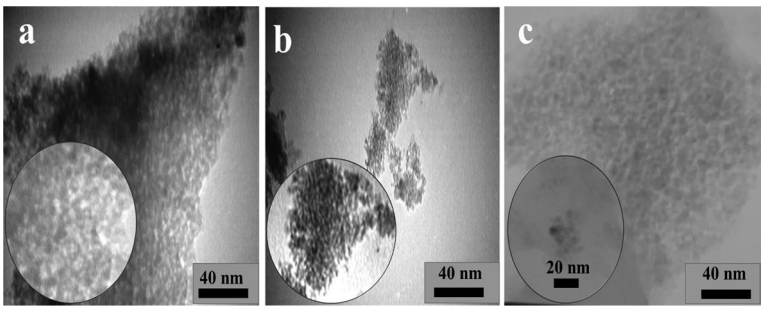

Fig. 5 TEM images of fabricated **a** Cdot, **b** Al_2O_3:Cr and **c** Al_2O_3:Cr/Cdot nanoparticles

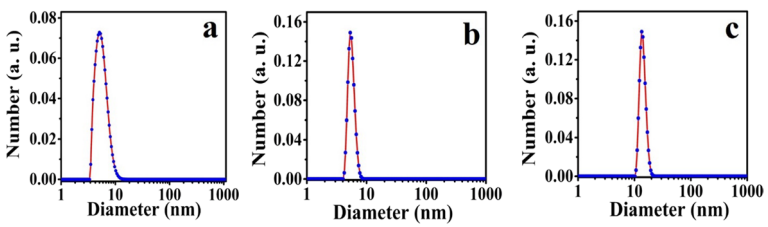

Fig. 6 DLS analysis of fabricated **a** Cdot, **b** Al_2O_3:Cr and **c** Al_2O_3:Cr/Cdot nanoparticles

the TEM data and underscore the high quality of the synthesized nanoparticles, which is crucial for their potential applications in various fields.

ROS evaluation

The potential of Al_2O_3:Cr/Cdot NPs in PDT for cancer treatment was investigated, with a focus on their ability to ROS and serve as effective photosensitizers. In PDT, the production of singlet oxygen is crucial for inducing cytotoxicity in cancer cells. This process involves the interaction between activated photosensitive molecules and oxygen molecules, leading to the generation of ROS. To assess ROS generation, anthracene was employed as a singlet oxygen detector, as it undergoes an oxidation process to form anthraquinone in the presence of ROS, leading to a decrease in its absorption intensity. To measure singlet oxygen production, an anthracene solution was exposed to UV light in the presence or absence of NPs. The UV–Vis absorption spectra of anthracene solutions with and without NPs before and after UVA light exposure were compared and results are presented in Fig. 7a. While individual anthracene solutions showed no significant changes in absorption spectra pre- and post-irradiation, a noticeable reduction was observed in the absorption spectra of anthracene solutions containing Al_2O_3:Cr NPs and Al_2O_3:Cr/Cdot NPs. This reduction indicated anthracene decomposition and anthraquinone production, signifying the generation of singlet oxygen facilitated by the NPs. Specifically, Al_2O_3:Cr/Cdot NPs exhibited higher emission intensity compared to Al_2O_3:Cr NPs and Al_2O_3 NPs, suggesting their superior ability to decompose anthracene and generate singlet oxygen.

Additionally, methylene blue (MB) was utilized to evaluate the concentration of hydroxyl free radicals. MB, known for its water solubility and stability under UV light exposure, can break down to release water and carbon dioxide during oxidation reactions triggered by hydroxyl radicals. The absorption spectrum of the MB solution with Al_2O3:Cr/Cdot NPs (Fig. 7b) showed a decrease in intensity compared to the solution without NPs, indicating the generation of hydroxyl radicals. The intensity of the UV–vis absorption spectrum of the MB solution containing Al_2O_3 NPs and Al_2O_3:Cr NPs was higher than that of the solution with Al_2O_3:Cr/Cdot NPs, suggesting a lower production of hydroxyl radicals in the latter (Fig. 7b). These findings underscore the potential of Al_2O_3:Cr/Cdot as promising agents for PDT in cancer therapy. These results align with findings from other studies investigating the photodynamic activity of various

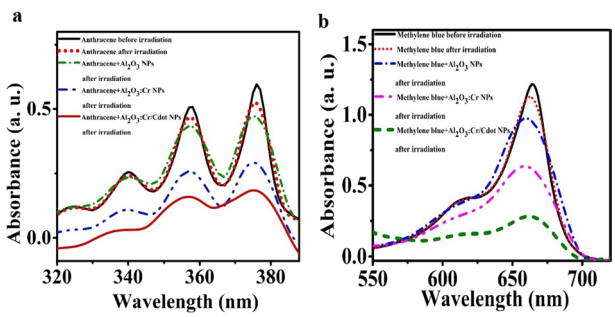

Fig. 7 UV–vis spectra obtained from: **a** anthracene solution, and **b** methylene blue solution without and with various NPs, before and after irradiation for 1 h

nanoparticles and photosensitizers. In a study investigating γ-Fe_2O_3 NPs complexes, a dose-dependent increase in intracellular ROS levels was observed under irradiation, indicating the efficient production of ROS upon exposure to light (Nistorescu et al. 2021). Similarly, investigations into the photodynamic activity of ZnO NPs revealed their ability to generate hydroxyl radicals under UV illumination, as evidenced by the characteristic electron paramagnetic resonance spectra of hydroxyl radical spin adducts. These findings suggest a common mechanism of ROS generation among different nanomaterials, emphasizing the significance of ROS in mediating the cytotoxic effects of PDT against cancer cells (Ancona et al. 2018). Furthermore, studies evaluating the singlet oxygen production of porphyrin-functionalized iron oxide nanoparticles (IONPs) demonstrated the essential role of photosensitizers in ROS generation for PDT. The anchoring of photosensitizer ligands onto the surface of IONPs significantly enhanced their capacity to generate singlet oxygen, highlighting the importance of nanoparticle design in optimizing ROS production for effective cancer therapy (Penon et al. 2016). Cdot has also gained attention as promising photosensitizers for PDT due to their unique optical properties and biocompatibility. In one study, Cdot were investigated for their photosensitivity and the results indicated that under UV light, Cdot showed superior efficiency in singlet oxygen production compared to a standard photosensitizer, attributed to their excellent water solubility (Yue et al. 2021). Similarly, investigations into the photodynamic activity of Mn-Cdot@FA/Ce6 nanohybrids revealed their ability to generate ROS upon laser irradiation, leading to a time-dependent decrease in the photoluminescence spectra of a molecular probe. The generated singlet oxygen in PDT was found to induce cytotoxic effects in cancer cells, highlighting the potential of Mn-Cdot@FA/Ce6 nanohybrids as effective photosensitizers for cancer therapy (Irmania et al. 2020). Overall, the findings from these studies corroborate the results of ROS evaluation for Al_2O_3:Cr/Cdot NPs, indicating their potential as effective photosensitizers for inducing cytotoxicity in cancer cells through ROS-mediated mechanisms.

Determination of the minimum inhibitory concentration (MIC) and the minimum bactericidal concentration (MBC)

The MIC and minimum bactericidal concentration MBC values were determined using the broth microdilution method to assess the antibacterial efficacy of the synthesized NPs against drug-resistant bacteria, including MRSA (*S. aureus* ATCC 43300) and *P. aeruginosa PAO1*. Table 1 summarizes the MIC and MBC values for the tested NPs. Among the tested NPs, Al_2O_3:Cr/Cdot NPs exhibited the most notable antibacterial activity, as evidenced by their lower MIC and MBC values compared to individual components. Specifically, the MIC values for Al_2O_3:Cr/Cdot against *S. aureus* ATCC 43300 and *P. aeruginosa PAO1* were approximately 3.41 μg/mL and 1.7 μg/mL, respectively. In contrast, higher MIC values were observed for Al_2O_3:Cr and Cdot alone, indicating reduced efficacy against these bacteria strains. The MBC values for Al_2O_3:Cr/Cdot against *S. aureus* ATCC 43300 and *P. aeruginosa PAO1* were approximately 9.33 μg/mL and 4.66 μg/mL, respectively. These values indicate that Al_2O_3:Cr/Cdot not only inhibit bacterial growth but also effectively kill the bacteria at low concentrations.

The antibacterial activity of the Al_2O_3:Cr/Cdot NPs is notable, likely resulting from the cooperative effect of the Al_2O_3:Cr and Cdot nanoparticles. The antibacterial effect

Table 1 Minimum inhibitory concentration (MIC) and minimum bactericidal concentration (MBC) values for standard strains of *S. aureus ATCC 43300* and *P. aeruginosa PAO1* treated with different NPs

Microorganisms	Al_2O_3:Cr		Cdot		Al_2O_3:Cr/Cdot	
	MIC (µg/mL)	MBC (µg/mL)	MIC (µg/mL)	MBC (µg/mL)	MIC (µg/mL)	MBC (µg/mL)
S. aureus ATCC 43300	13.03 ± 0.057^{c}	26 ± 0.05^{c}	1000 ± 0.13^{a}	1000 ± 0.1^{a}	3.41 ± 0.14^{d}	9.33 ± 4^{d}
P.aeruginosa PAO1	13.50 ± 0.050^{c}	26.15 ± 0.26^{c}	250 ± 12.5^{b}	500 ± 25^{b}	1.7 ± 0.05^{e}	4.66 ± 2^{e}

Significant differences ($p<0.05$) among MIC values are indicated by distinct lowercase letters (a, b, c, d, e) and among MBC values by lowercase prime letters (a′, b′, c′, d′, e′). If two variables share the same letter, their means are not statistically significantly different. Conversely, if they have different letters, the difference between their means is statistically significant

MIC and MBC values are expressed in micrograms per milliliter (µg/mL). Al_2O_3:Cr: chromium-doped aluminum oxide nanoparticles; Cdot: carbon quantum dots; Al_2O_3:Cr/Cdot NPs: chromium-doped aluminum oxide nanoparticles decorated with carbon quantum dots. The values represent the concentration at which the growth of bacteria was inhibited (MIC) and killed (MBC) by the respective NPs. Higher values indicate higher resistance of the bacteria to the treatment

of Alumina is attributed to two main mechanisms. First, electrostatic attraction between the nanoparticles and the bacterial outer membrane or cell wall can lead to bacterial death by altering membrane permeability. Additionally, the formation of ROS disrupts bacterial life by inducing destruction (Gudkov et al. 2022). Recent studies have shown increased intracellular ROS levels in *Escherichia coli* (*E. coli*) after exposure to Al_2O_x NPs for two hours. Moreover, the antibacterial effect involves Al^{3+} bonding with the phospholipids of the cell wall, disrupting enzyme activity and receptors, and rearranging the lipid membrane, ultimately leading to cell death (Khashan et al. 2020). Jwad et al. (2019), demonstrated that Al_2O_3 NPs hindered the growth of *E. coli*, *P. aeruginosa*, and *S. aureus*, with gram-negative bacteria exhibiting greater resilience than gram-positive bacteria. In a separate study, the antibacterial effects of Al_2O_3, Ag, and Al_2O_3/Ag thin films on *Pseudomonas putida* (*P. putida*) and *E. coli* were investigated. While the combination of an Al_2O_3 and Ag bilayer film had a stronger antibacterial effect on *P. putida* than either Al_2O_3 or Ag alone, there was no significant effect on *E. coli*. This phenomenon may result from the formation of oxidizing substances upon contact of the bacterial suspension with the surface, accounting for the antimicrobial activity of the bilayer film on *P. putida* and *E. coli* (Angelov et al. 2016). Additionally, a study determined that synthesized Au:SnO_2/Cdot NPs exhibited increased antibacterial activity compared to Au:SnO_2 alone. The research showed that Au:SnO_2/Cdot NPs displayed superior antibacterial properties compared to Au:SnO_2, attributed to the enhancement in antibacterial activity due to the optical properties of Cdot NPs, which produce more ROS, thereby increasing antibacterial efficacy (Wu et al. 2021; Roomi et al. 2021).

Anti-biofilm activity of Al_2O_3:Cr/Cdot NPs against *MRSA* and *P. aeruginosa PAO1* biofilm

The microtiter plate technique was employed to evaluate the effect of Al_2O_3:Cr/Cdot NPs on biofilm formation in *S. aureus* ATCC 43300 and *P. aeruginosa PAO1*PAO1. Figure 8 illustrates the effectiveness of different concentrations of Al_2O_3:Cr/Cdot NPs in preventing biofilm formation. The observed effect varied depending on the dosage, with the most significant reduction in biofilm formation occurring at higher concentrations (MIC). Specifically, the MIC concentration led to an inhibition rate of 89% and 95% for MRSA and *P. aeruginosa PAO1*, respectively.

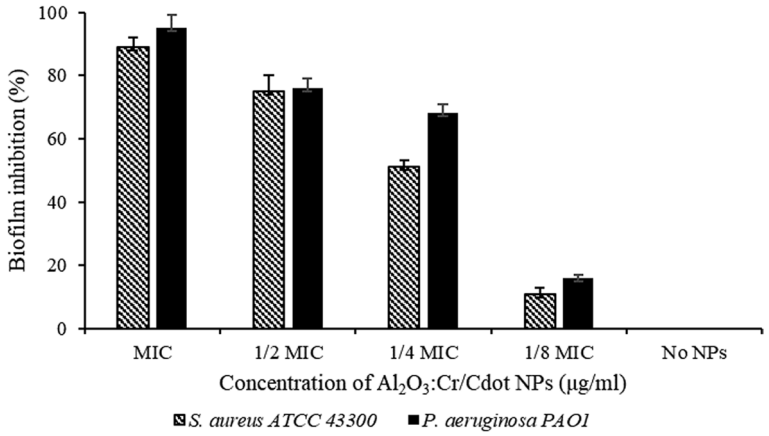

Fig. 8 The inhibition of biofilm formation by *S. aureus ATCC 43300* and *P. aeruginosa PAO1* treated with sub-MIC and MIC concentrations of Al_2O_3:Cr/Cdot NPs. The inhibition rate is expressed as a percentage

Several other studies have also investigated the efficacy of various NPs and PDT approaches in targeting biofilms formed by different bacterial pathogens, providing valuable insights into potential therapeutic interventions. One study focused on polyamine-functionalized Cdot, demonstrating enhanced antibacterial activity, particularly against mature *S. aureus* biofilms (Li et al. 2020). Another investigation developed multifunctional NPs containing Chlorin e6 (Ce6), Coumarin 6 (C6), and Fe_3O_4 NPs for antibacterial PDT against periodontitis-related pathogens. The NPs exhibited strong anti-biofilm activity, with excellent biocompatibility and targeting capabilities (Sun et al. 2019). Similarly, antimicrobial PDT using nano-chitosan encapsulated indocyanine green (CNPs/ICG) showed a significant reduction in the viability, biofilm formation capacity, and metabolic activity of *Aggregatibacter Actinomycetemcomitans*, a common etiological agent in periodontitis and peri-implantitis. This approach also downregulated virulent gene expression, indicating its potential for treating *A. actinomycetemcomitans* infections (Pourhajibagher et al. 2018). Furthermore, the combination of indocyanine green (ICG) with superparamagnetic iron oxide NPs (SPIONs) demonstrated synergistic antibacterial and antibiofilm effects against Gram-negative and Gram-positive bacteria (Bilici et al. 2020). Moreover, PDT with MB and gold NPs (AuNPs) showed antibacterial and anti-biofilm effects against *S. mutans*, an important cariogenic bacterial agent. While traditional PDT with MB alone was effective, the addition of AuNPs did not significantly enhance its efficacy, suggesting that the routine PDT approach remains a viable option (Lavaee et al. 2021). Biofilms represent a significant challenge in clinical settings due to their increased resistance to antimicrobial agents compared to planktonic bacteria. This resistance is primarily attributed to the presence of an extracellular matrix, which acts as a protective barrier, limiting the penetration of antimicrobial agents into the biofilm structure. Traditional antibiotic therapies often fail to eradicate biofilms completely, leading to persistent infections and contributing to the development of antibiotic resistance. In this context, the inhibitory effects of Al_2O_3:Cr/Cdot NPs on biofilm formation hold considerable promise for combating antibiotic resistance associated with biofilms. These NPs possess multifunctional properties that synergistically target various aspects of biofilm development and bacterial survival mechanisms. The extracellular matrix

plays a crucial role in maintaining the structural integrity of biofilms and protecting bacterial cells from environmental stresses and antimicrobial agents. Al_2O_3:Cr/Cdot NPs may disrupt this matrix through electrostatic interactions and physical disruption, leading to the destabilization of biofilm architecture (Pinto et al. 2020). Alumina nanoparticles, along with the photosensitizing properties of carbon quantum dots, can interact with bacterial membranes, leading to membrane destabilization and permeabilization. This disruption compromises the integrity of the bacterial membrane, resulting in leakage of intracellular contents and ultimately bacterial cell death (Wang et al. 2017). The photosensitizing properties of Cdot enable the generation ROS upon exposure to light. ROS, such as singlet oxygen and hydroxyl radicals, possess potent antimicrobial activity and can induce oxidative damage to bacterial cells, including lipid peroxidation, protein oxidation, and DNA damage (Paramanantham et al. 2019). By targeting these key pathways, Al_2O_3:Cr/Cdot NPs effectively inhibit biofilm formation and eradicate established biofilms, offering a promising strategy for combating biofilm-associated infections, thus presenting a promising avenue for future research and clinical applications in the field of antimicrobial therapy.

Anticancer activity of Al_2O_3:Cr/Cdot NPs

To evaluate the anticancer effect of Al_2O_3:Cr/Cdot NPs in combination with UVA exposure, C26 cells were utilized as a model system. The experimental groups included: (1) C26 cells exposed to UVA light, (2) C26 cells treated with Al_2O_3:Cr/Cdot NPs, and (3) C26 cells treated with Al_2O_3:Cr/Cdot NPs followed by UVA exposure. Initially, C26 cells were exposed to UVA light, and cell viability was measured after 10 min. Surprisingly, UVA exposure alone did not exhibit any significant effect on cell viability, with viability remaining at 100%. This observation suggests that UVA light, at the given intensity and duration, did not induce cytotoxicity in C26 cells under the experimental conditions. Subsequently, the viability of C26 cells treated with Al_2O_3:Cr/Cdot NPs was assessed (Fig. 9). The half-maximal inhibitory concentration (IC50) of Al_2O_3:Cr/Cdot NPs was determined to be 20 µg/mL, indicating their inherent cytotoxicity against C26 cancer cells. Remarkably, when C26 cells were treated with Al_2O_3:Cr/Cdot NPs and exposed to UVA light, a significant enhancement in cytotoxicity was observed compared to

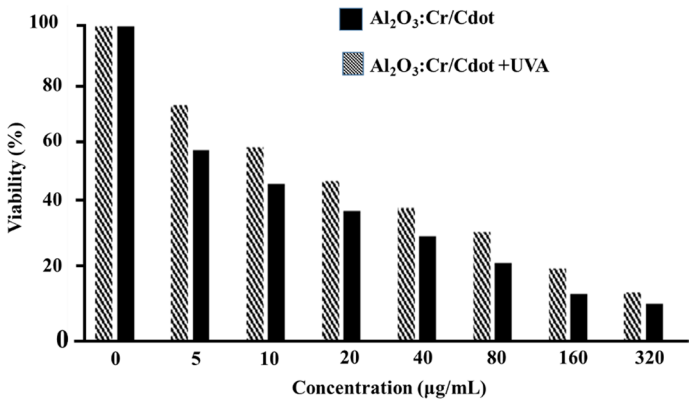

Fig. 9 Cell viability. The IC50 of both Al_2O_3:Cr/Cdot NPs and Al_2O_3:Cr/Cdot NPs + UVA for C26 cell line has been shown by concentration(µg/mL)

treatment with NPs alone. The IC50 value for Al_2O_3:Cr/Cdot NPs combined with UVA light decreased to 10 μg/mL, demonstrating a pronounced increase in cytotoxicity. These results underscore the potential of UVA light to augment the anticancer efficacy of Al_2O_3:Cr/Cdot NPs, highlighting the synergistic effect of nanoparticle-mediated cytotoxicity and photodynamic therapy. The mechanism underlying this enhanced cytotoxicity may involve the generation of ROS by Al_2O_3:Cr/Cdot NPs upon UVA exposure, leading to increased oxidative stress and cell death in cancer cells. The results of the anticancer activity of Al_2O_3:Cr/Cdot NPs combined with UVA exposure reveal a promising avenue for cancer therapy. These findings align with recent research efforts focused on developing nanomaterial-based PDT strategies for cancer treatment. Studies investigating the use of various photosensitizers, such as lipophilic chalcogen tetrasubstituted zinc (II) phthalocyanines and iron oxide loaded porphyrin-grafted lipid nanoparticles (Fe_3O_4@PGL NPs), have demonstrated their efficacy in inducing cytotoxic effects against cancer cells upon light activation. The enhanced photodynamic effects observed in these studies underscore the potential of nanomaterials to serve as effective agents for targeted cancer therapy (Ezquerra Riega et al. 2022; Liang et al. 2021). Metal-based nanoparticles, including zinc oxide nanoparticles (ZnO-NPs) and NiO nanoparticles, have also shown promising cytotoxicity against cancer cells under UV irradiation, attributed to the generation of ROS during PDT. This ROS-mediated cell death pathway highlights the importance of photoactivation in enhancing the anticancer activity of nanomaterials (Ismail et al. 2014). Furthermore, the comparison between titanium dioxide (TiO_2) and zinc oxide (ZnO) nanoparticles as photosensitizers in PDT emphasizes the role of ROS generation in eliciting anticancer effects. Both TiO_2 and ZnO nanoparticles were found to induce ROS-mediated apoptosis in tumor cells upon irradiation, supporting their potential as effective agents for PDT-based cancer therapy (Zhang et al. 2014). The synergistic effect observed between Al_2O_3:Cr/Cdot NPs and UVA exposure underscores the importance of ROS-mediated mechanisms in enhancing anticancer efficacy. The ability of UVA light to augment the cytotoxic effects of Al_2O_3:Cr/Cdot NPs suggests a promising strategy for improving the therapeutic outcomes of cancer treatment.

Conclusion

This study focused on synthesizing and characterizing Cr-doped Al_2O_3-carbon quantum dot nanoparticles (Al_2O_3:Cr/Cdot NPs) and investigating their antibacterial and anticancer properties. In conclusion, the synthesis and characterization of Al_2O_3:Cr/Cdot NPs have been successfully demonstrated. XRD analysis confirmed the crystalline structure of the nanoparticles, with distinct peaks corresponding to Al_2O_3 and Cdot components. EDS analysis revealed the elemental composition of the nanoparticles, confirming the presence of aluminum, oxygen, chromium, and carbon atoms in the desired nanocomposite material. FTIR spectroscopy provided insights into the chemical bonds and interactions within the nanoparticles, illustrating successful bonding between Cdot and Al_2O_3:Cr NPs. Morphological analysis via SEM and TEM showed well-defined spherical nanoparticles with minimal agglomeration, indicative of high-quality synthesis. The evaluation of ROS generation demonstrated the potential of Al_2O_3:Cr/Cdot NPs in PDT for cancer treatment. The NPs exhibited superior ability to decompose anthracene and

generate singlet oxygen, highlighting their efficacy as photosensitizers. Additionally, the production of hydroxyl radicals further supported their cytotoxic effects on cancer cells.

The antibacterial activity of Al_2O_3:Cr/Cdot NPs was notable, with lower MIC and MBC values compared to individual components. The nanoparticles effectively inhibited bacterial growth and biofilm formation, offering a promising strategy against drug-resistant bacteria. Moreover, the enhanced cytotoxicity of Al_2O_3:Cr/Cdot NPs in combination with UVA exposure underscored their potential in cancer therapy. Overall, the results indicate the significant potential of Al_2O_3:Cr/Cdot NPs as multifunctional agents for addressing antibiotic resistance, inhibiting biofilm formation, and combating cancer. The synergistic effects observed in various applications highlight the versatility and promising prospects of these nanoparticles in biomedical research and clinical practice. Further exploration of their therapeutic efficacy and mechanisms of action could lead to the development of advanced treatment strategies for infectious diseases and cancer.

Acknowledgements
Not applicable.

Author contributions
The authors confirm contributions to this paper as follows: Investigation and database searching, writing, and draft preparation: Merat Karimi, Mina Homayoonfal, Ehsan Sadeghi, Mostafa Zahedifar, Reyhaneh Adibi, Majid Nejati, Bahareh Mohammadzadeh, Amirreza Ostadian, Mahsa Khabraghi, Arash Raisi, Fatemeh Ravaei, Somaye Rashki Review and editing and validation: Michael R Hamblin, and Hamed Mirzaei. Supervision and project administration: Hamed Mirzaei.

Funding
Not applicable.

Availability of data and materials
Not applicable.

Declarations

Ethics approval and consent to participate
Not applicable.

Consent for publication
Not applicable.

Competing interests
The authors declare no conflict of interest.

Author details
[1]Institute of Nanoscience and Nanotechnology, University of Kashan, Kashan, Iran. [2]Research Center for Biochemistry and Nutrition in Metabolic Diseases, Institute for Basic Sciences, Kashan University of Medical Sciences, Kashan, Iran. [3]Department of Physics, University of Kashan, Kashan, Isfahan, Iran. [4]Department of Laboratory Medicine, School of Allied Medical Sciences, Kashan University of Medical Sciences, Kashan, Iran. [5]Student Research Committee, Kashan University of Medical Sciences, Kashan, Islamic Republic of Iran. [6]Department of Midwifery, Faculty of Nursing and Midwifery, Pregnancy Health Research Center, Zahedan University of Medical Sciences, Zahedan, Iran. [7]Physiology Research Center, Institute for Basic Sciences, Kashan University of Medical Sciences, Kashan, Iran. [8]Laser Research Centre, Faculty of Health Science, University of Johannesburg, Doornfontein 2028, South Africa. [9]Anatomical Sciences Research Center, Institute for Basic Sciences, Kashan University of Medical Sciences, Kashan, Iran.

Received: 16 November 2023 Accepted: 17 April 2024
Published online: 03 June 2024

References

Adamczyk A, Długoń E (2012) The FTIR studies of gels and thin films of Al_2O_3–TiO_2 and Al_2O_3–TiO_2–SiO_2 systems. Spectrochim Acta Part A Mol Biomol Spectrosc 89:11–17

Ahmed Mohamed HE, Afridi S, Khalil AT, Zohra T, Ali M, Alam MM et al (2020) Phyto-fabricated Cr_2O_3 nanoparticle for multifunctional biomedical applications. Nanomedicine 15(17):1653–1669

Algarra M, González-Calabuig A, Radotić K, Mutavdzic D, Ania C, Lázaro-Martínez JM et al (2018) Enhanced electrochemical response of carbon quantum dot modified electrodes. Talanta 178:679–685

Anand A, Unnikrishnan B, Wei S-C, Chou CP, Zhang L-Z, Huang C-C (2019) Graphene oxide and carbon dots as broad-spectrum antimicrobial agents—a minireview. Nanoscale Horizons 4(1):117–137
Ancona A, Dumontel B, Garino N, Demarco B, Chatzitheodoridou D, Fazzini W et al (2018) Lipid-coated zinc oxide nanoparticles as innovative ROS-generators for photodynamic therapy in cancer cells. Nanomaterials 8(3):143
Angelov O, Stoyanova D, Ivanova I, Todorova S (eds) (2016) Antimicrobial effect of Al_2O_3, Ag and Al_2O_3/Ag thin films on Escherichia coli and Pseudomonas putida. In: Journal of Physics: Conference Series. IOP Publishing
Babaei P, Safai-Ghomi J, Rashki S (2022) Engineered dual-purpose Ta-doped ZnO/hydroxyapatite nanocomposites: antibacterial activity and robust catalyst in MW-induced synthesis of chromopyrimidines. Ceram Int 48(6):8359–8373
Bilici K, Atac N, Muti A, Baylam I, Dogan O, Sennaroglu A et al (2020) Broad spectrum antibacterial photodynamic and photothermal therapy achieved with indocyanine green loaded SPIONs under near infrared irradiation. Biomater Sci 8(16):4616–4625
Chinemerem Nwobodo D, Ugwu MC, Oliseloke Anie C, Al-Ouqaili MT, Chinedu Ikem J, Victor Chigozie U et al (2022) Antibiotic resistance: the challenges and some emerging strategies for tackling a global menace. J Clin Lab Anal 36(9):e24655
Dolmans DE, Fukumura D, Jain RK (2003) Photodynamic therapy for cancer. Nat Rev Cancer 3(5):380–387
Dutt Y, Dhiman R, Singh T, Vibhuti A, Gupta A, Pandey RP et al (2022) The association between biofilm formation and antimicrobial resistance with possible ingenious bio-remedial approaches. Antibiotics 11(7):930
Ezquerra Riega SD, Valli F, Rodríguez HB, Marino J, Roguin LP, Lantaño B et al (2022) Chalcogen bearing tetrasubstituted zinc (II) phthalocyanines for CT26 colon carcinoma cells photodynamic therapy. Dyes Pigm 201:110110
Gudkov SV, Burmistrov DE, Smirnova VV, Semenova AA, Lisitsyn AB (2022) A mini review of antibacterial properties of Al_2O_3 nanoparticles. Nanomaterials 12(15):2635
Hao X, Huang L, Zhao C, Chen S, Lin W, Lin Y et al (2021) Antibacterial activity of positively charged carbon quantum dots without detectable resistance for wound healing with mixed bacteria infection. Mater Sci Eng C 123:111971
Hong EJ, Choi DG, Shim MS (2016) Targeted and effective photodynamic therapy for cancer using functionalized nanomaterials. Acta Pharm Sin B 6(4):297–307
Hsu P-C, Chen P-C, Ou C-M, Chang H-Y, Chang H-T (2013) Extremely high inhibition activity of photoluminescent carbon nanodots toward cancer cells. J Mater Chem B 1(13):1774–1781
Irmania N, Dehvari K, Gedda G, Tseng PJ, Chang JY (2020) Manganese-doped green tea-derived carbon quantum dots as a targeted dual imaging and photodynamic therapy platform. J Biomed Mater Res B Appl Biomater 108(4):1616–1625
Ismail AFM, Ali MM, Ismail LFM (2014) Photodynamic therapy mediated antiproliferative activity of some metal-doped ZnO nanoparticles in human liver adenocarcinoma HepG2 cells under UV irradiation. J Photochem Photobiol B 138:99–108
Jwad KH, Saleh TH, Abd-Alhamza B (2019) Preparation of Aluminum oxide nanoparticles by laser ablation and a study of their applications as antibacterial and wounds healing agent. Nano Biomed Eng 11(3):313–319
Karagianni A, Tsierkezos NG, Prato M, Terrones M, Kordatos KV (2023) Application of carbon-based quantum dots in photodynamic therapy. Carbon 203:273–310
Karami M, Ghanbari M, Alshamsi HA, Rashki S, Salavati-Niasari M (2021) Facile fabrication of Tl_4HgI_6 nanostructures as novel antibacterial and antibiofilm agents and photocatalysts in the degradation of organic pollutants. Inorg Chem Front 8(10):2442–2460
Karimi M, Kashi MA, Montazer AH (2021) Synthesis and characterization of ultrafine γ-Al_2O_3:Cr nanoparticles and their performance in antibacterial activity. J Sol–gel Sci Technol 99(1):178–187
Khan MF, Hameedullah M, Ansari AH, Ahmad E, Lohani M, Khan RH et al (2014) Flower-shaped ZnO nanoparticles synthesized by a novel approach at near-room temperatures with antibacterial and antifungal properties. Int J Nanomed 9:853–864
Khan MF, Ansari AH, Hameedullah M, Ahmad E, Husain FM, Zia Q et al (2016) Sol–gel synthesis of thorn-like ZnO nanoparticles endorsing mechanical stirring effect and their antimicrobial activities: potential role as nano-antibiotics. Sci Rep 6(1):1–12
Khashan KS, Sulaiman GM, Hussain SA, Marzoog TR, Jabir MS (2020) Synthesis, characterization and evaluation of antibacterial, anti-parasitic and anti-cancer activities of aluminum-doped zinc oxide nanoparticles. J Inorg Organomet Polym Mater 30(9):3677–3693
Lavaee F, Motamedifar M, Rafiee G (2021) The effect of photodynamic therapy by gold nanoparticles on *Streptococcus mutans* and biofilm formation: an in vitro study. Lasers Med Sci 37:1–9
Li P, Yang X, Zhang X, Pan J, Tang W, Cao W et al (2020) Surface chemistry-dependent antibacterial and antibiofilm activities of polyamine-functionalized carbon quantum dots. J Mater Sci 55:16744–16757
Liang X, Chen M, Bhattarai P, Hameed S, Tang Y, Dai Z (2021) Complementing cancer photodynamic therapy with ferroptosis through iron oxide loaded porphyrin-grafted lipid nanoparticles. ACS Nano 15(12):20164–20180
Nistorescu S, Udrea A-M, Badea MA, Lungu I, Boni M, Tozar T et al (2021) Low blue dose photodynamic therapy with porphyrin-iron oxide nanoparticles complexes: in vitro study on human melanoma cells. Pharmaceutics 13(12):2130
Paramanantham P, Anju V, Dyavaiah M, Siddhardha B (2019) Applications of carbon-based nanomaterials for antimicrobial photodynamic therapy. Microbial nanobionics: volume 2, basic research and applications. Springer, Cham, pp 237–259
Penon O, Marín MJ, Amabilino DB, Russell DA, Pérez-García L (2016) Iron oxide nanoparticles functionalized with novel hydrophobic and hydrophilic porphyrins as potential agents for photodynamic therapy. J Colloid Interface Sci 462:154–165
Pinto RM, Soares FA, Reis S, Nunes C, Van Dijck P (2020) Innovative strategies toward the disassembly of the EPS matrix in bacterial biofilms. Front Microbiol 11:535344
Pourhajibagher M, Rokn AR, Rostami-Rad M, Barikani HR, Bahador A (2018) Monitoring of virulence factors and metabolic activity in *Aggregatibacter actinomycetemcomitans* cells surviving antimicrobial photodynamic therapy via nano-chitosan encapsulated indocyanine green. Front Phys 6:124

Prasad R, Aiyer S, Chauhan DS, Srivastava R, Selvaraj K (2016) Bioresponsive carbon nano-gated multifunctional mesoporous silica for cancer theranostics. Nanoscale 8(8):4537–4546
Prathumsuwan T, Jamnongsong S, Sampattavanich S, Paoprasert P (2018) Preparation of carbon dots from succinic acid and glycerol as ferrous ion and hydrogen peroxide dual-mode sensors and for cell imaging. Opt Mater 86:517–529
Raikwar V (2022) Synthesis and study of carbon quantum dots (CQDs) for enhancement of luminescence intensity of CQD@$LaPO_4$:Eu^{3+} nanocomposite. Mater Chem Phys 275:125277
Ramasamy M, Lee J (2016) Recent nanotechnology approaches for prevention and treatment of biofilm-associated infections on medical devices. BioMed Res Int. https://doi.org/10.1155/2016/1851242
Ramesh C, Mohan Kumar K, Latha N, Ragunathan V (2012) Green synthesis of Cr_2O_3 nanoparticles using *Tridax procumbens* leaf extract and its antibacterial activity on *Escherichia coli*. Curr Nanosci 8(4):603–607
Roomi AB, Widjaja G, Savitri D, Turki Jalil A, Fakri Mustafa Y, Thangavelu L et al (2021) SnO_2: Au/carbon quantum dots nanocomposites: synthesis, characterization, and antibacterial activity. J Nanostruct 11(3):514–523
Safardoust-Hojaghan H, Salavati-Niasari M, Amiri O, Rashki S, Ashrafi M (2021) Green synthesis, characterization and antimicrobial activity of carbon quantum dots-decorated ZnO nanoparticles. Ceram Int 47(4):5187–5197
Sarkar N, Sahoo G, Das R, Prusty G, Swain SK (2017) Carbon quantum dot tailored calcium alginate hydrogel for pH responsive controlled delivery of vancomycin. Eur J Pharm Sci 109:359–371
Sun X, Wang L, Lynch CD, Sun X, Li X, Qi M et al (2019) Nanoparticles having amphiphilic silane containing Chlorin e6 with strong anti-biofilm activity against periodontitis-related pathogens. J Dent 81:70–84
Tavakkoli F, Zahedifar M, Sadeghi E (2018) Effect of LaF3: Ag fluorescent nanoparticles on photodynamic efficiency and cytotoxicity of Protoporphyrin IX photosensitizer. Photodiagn Photodyn Ther 21:306–311
Umar K, Mfarrej MFB, Rahman QI, Zuhaib M, Khan A, Zia Q et al (2022) ZnO nano-swirlings for Azo Dye AR183 photocatalytic degradation and antimycotic activity. Sci Rep 12(1):14023
Vuotto C, Donelli G (2019) Novel treatment strategies for biofilm-based infections. Drugs 79:1635–1655
Wang T-Y, Libardo MDJ, Angeles-Boza AM, Pellois J-P (2017) Membrane oxidation in cell delivery and cell killing applications. ACS Chem Biol 12(5):1170–1182
Wu Y, Li C, van der Mei HC, Busscher HJ, Ren Y (2021) Carbon quantum dots derived from different carbon sources for antibacterial applications. Antibiotics 10(6):623
Yue J, Li L, Jiang C, Mei Q, Dong W-F, Yan R (2021) Riboflavin-based carbon dots with high singlet oxygen generation for photodynamic therapy. J Mater Chem B 9(38):7972–7978
Zhang H, Shan Y, Dong L (2014) A comparison of TiO_2 and ZnO nanoparticles as photosensitizers in photodynamic therapy for cancer. J Biomed Nanotechnol 10(8):1450–1457

Publisher's Note